

Dynamics of GN-z11 Explored by JWST Integral Field Spectroscopy: Gaseous Rotating Disk at $z = 10.60$ Suggestive of Weak Feedback?

YI XU,^{1,2} MASAMI OUCHI,^{3,1,4,5} HIDENOBU YAJIMA,⁶ HAJIME FUKUSHIMA,⁶ YUICHI HARIKANE,¹ YUKI ISOBE,⁷
KIMIIHIKO NAKAJIMA,³ MINAMI NAKANE,^{1,8} YOSHIAKI ONO,¹ HIROYA UMEDA,^{1,8} HIROTO YANAGISAWA,^{1,8} AND
YECHI ZHANG^{3,1,2,5}

¹*Institute for Cosmic Ray Research, The University of Tokyo, 5-1-5 Kashiwanoha, Kashiwa, Chiba 277-8582, Japan*

²*Department of Astronomy, Graduate School of Science, the University of Tokyo, 7-3-1 Hongo, Bunkyo, Tokyo 113-0033, Japan*

³*National Astronomical Observatory of Japan, 2-21-1 Osawa, Mitaka, Tokyo 181-8588, Japan*

⁴*Graduate University for Advanced Studies (SOKENDAI), 2-21-1 Osawa, Mitaka, Tokyo 181-8588, Japan*

⁵*Kavli Institute for the Physics and Mathematics of the Universe (Kavli IPMU, WPI), The University of Tokyo, 5-1-5 Kashiwanoha, Kashiwa, Chiba, 277-8583, Japan*

⁶*Center for Computational Sciences, University of Tsukuba, Tennodai, 1-1-1 Tsukuba, Ibaraki 305-8577, Japan*

⁷*Waseda Research Institute for Science and Engineering, Faculty of Science and Engineering, Waseda University, 3-4-1, Okubo, Shinjuku, Tokyo 169-8555, Japan*

⁸*Department of Physics, Graduate School of Science, The University of Tokyo, 7-3-1 Hongo, Bunkyo, Tokyo 113-0033, Japan*

(Received —; Revised —; Accepted —)

ABSTRACT

We investigate the dynamics of GN-z11, a luminous galaxy at $z = 10.60$, carefully analyzing the public deep integral field spectroscopy (IFS) data taken with JWST NIRSpec IFU. While the observations of the IFS data originally targeted a HeII clump near GN-z11, we find that CIII] $\lambda\lambda 1907, 1909$ emission from ionized gas at GN-z11 is bright and spatially extended significantly beyond the point-spread function (PSF) in contrast with the GN-z11's compact UV-continuum morphology. The spatially extended CIII] emission of GN-z11 shows a velocity gradient, red- and blue-shifted components in the NE and SW directions, respectively, which cannot be explained by the variation of [CIII] $\lambda 1907$ /CIII] $\lambda 1909$ line ratios. We perform forward modeling with GalPak^{3D}, including the effects of PSF smearing and line blending, and find that the best-fit model is a nearly edge-on disk with a rotation velocity of $v_{\text{rot}} = 376_{-151}^{+110}$ km s⁻¹, a velocity dispersion of $\sigma_v = 113_{-48}^{+24}$ km s⁻¹, and a ratio of $v_{\text{rot}}/\sigma_v = 3.3_{-1.5}^{+1.7}$, indicative of a rotation-dominated disk at $z = 10.6$. Interestingly, the disk rotation velocity is faster than the circular velocity at the virial radius, $v_c(r_{200}) = 205_{-34}^{+28}$ km s⁻¹, estimated from the stellar mass, suggesting a compact disk produced under weak feedback such predicted in numerical simulations. In fact, the half-light radius of the CIII] emitting gas disk is only 294 ± 45 pc, while the one of the stellar UV component is even smaller, 196 ± 12 pc. While higher S/N data are necessary for a conclusion, these observational results would suggest that GN-z11 has a fast-rotating gaseous disk whose center possesses luminous stellar components or AGN providing weak feedback.

Keywords: galaxies: evolution — galaxies: kinematics and dynamics

1. INTRODUCTION

Primordial galaxies evolve into the various types of galaxies we see today involving complex interplay between different processes: accretion of cold gas, mi-

nor and major mergers, stellar and active-galactic-nuclei feedback (e.g., Dekel et al. 2009; Hopkins et al. 2012; Naab & Ostriker 2017; Nelson et al. 2019). On the other hand, many of these baryonic processes operate on physical scales that are well below the resolution of current cosmological simulations, and are mostly calibrated to match observations in the local Universe, leaving potential crisis to explain galaxy evolution in the early uni-

verse. Spatially resolved studies of the gas kinematics can be critical to give a consistent picture of how galaxies grow and evolve across cosmic time.

Ground-based surveys using near-infrared integral field unit (IFU) such as SINS (Förster Schreiber et al. 2009; Genzel et al. 2011) and KMOS^{3D} (Wisnioski et al. 2015) provide rich dataset of gas kinematics for star forming galaxies at $z \sim 2$. Sub-millimeter observations using ALMA show great potential of investigating gas kinematics at $z > 4$. Neeleman et al. (2020); Rizzo et al. (2020, 2021) analyze the kinematics of $z \sim 4 - 5$ galaxies and reveal the existence of rotation-dominated disk in the early universe whose rotation velocity v_{rot} and be as high as ten times of the velocity dispersion σ_v . Parlanti et al. (2023) further report rotating but turbulent disks at $z > 5$ while Tokuoka et al. (2022) identify a potentially rotating disk at $z \sim 9$. After the launch of JWST, gas kinematics has been investigated for $z \sim 5 - 8$ galaxies using rest-frame optical emission observed by JWST NIRSpec MSA (de Graaff et al. 2023) and NIRCam WFSS (Nelson et al. 2023; Li et al. 2023).

Recent JWST observations provide deep spectroscopic data that reveals the properties of $z > 10$ galaxies (e.g., Arrabal Haro et al. 2023a,b; Curtis-Lake et al. 2023; Harikane et al. 2024). GN-z11 is a remarkably luminous high- z galaxies initially identified by Bouwens et al. (2010); Oesch et al. (2016). Recent JWST observations measure a spectroscopic redshift of 10.603. The NIRCam images reveal the compact size of GN-z11 (Tachella et al. 2023) while the NIRSpec IFU observations identify extended emission (Maiolino et al. 2023; Scholtz et al. 2023). Exploiting the spatial and spectral resolution of 3-dimensional (3d) IFU data, directly analyzing gas kinematics at $z > 10$ becomes possible.

In this paper, we analyze the the public data of GN-z11 taken with JWST NIRSpec IFU. While the observations of the IFS data originally targeted a He II clump near GN-z11, we find that CIII] $\lambda\lambda 1907, 1909$ emission at GN-z11 is bright and spatially extended, which traces the kinematics of ionized gas. This paper is structured as follows. Section 2 explains our observations and dataset. Section 3 describes how we analyze the morphology and kinematics of CIII] emission. We discuss and summarize our findings in Sections 4 and 5, respectively. Throughout the paper we adopt a Planck flat Λ CDM cosmology with $H_0 = 67.7 \text{ km s}^{-1} \text{ Mpc}^{-1}$ and $\Omega_m = 0.310$ (Planck Collaboration et al. 2020).

2. OBSERVATIONS AND DATA REDUCTIONS

In this work we use the data obtained by the NIRSpec IFU (Jakobsen et al. 2022; Böker et al. 2022) on JWST. The data was obtained on 22nd – 23rd of

May 2023 under the DDT program 4426 (PI: Roberto Maiolino). Details of the observations are presented in Maiolino et al. (2023). The observational setup utilised a medium cycling pattern of 10 dithers for a total integration time on source of 10.6 h with the medium-resolution grating/filter pair G235M/F170LP, and 3.3 h with the medium-resolution grating/filter pair G140M/F100LP. These configurations cover the spectral ranges of 0.97–1.89 and 1.66–3.17 μm , with a nominal spectral resolution of $R \sim 1000$.

We process the data taken with the grating/filter pair G235M/F170LP using the JWST Science Calibration pipeline version 1.12.5 under CRDS context `jwst_1170.pmap`. We make several modifications to the JWST pipeline to increase data quality, which we summarize here. The raw data files are downloaded from the MAST archive and processed with `calwebb_detector1`. The resulting count-rate frames are corrected for 1/f noise using `NSClean` (Rauscher 2024). We make a customized mask to obtain dark areas that are used to fit a background in Fourier space. We then perform the default pipeline steps including wcs-correction, flat-fielding, flux-calibrations, and building 3d data cubes through `calwebb_spec2`. We do not apply the `calwebb_spec3` process for detecting outliers and stacking frames as we find the data artefacts cannot be perfectly removed (see e.g., Perna et al. 2023; D’Eugenio et al. 2023). We utilize a customized median stacking to combine the 3d data cubes instead of the “drizzle” method of `calwebb_spec3`, which is inspired by the procedure taken by Vayner et al. (2023). The 3d data cube of each exposure frame is firstly subtracted by background and continuum following the method in Maiolino et al. (2023). We then use the `reproject` package (Robitaille et al. 2023) and the `reproject_interp` routine to align the different exposure frames for further median stacking. We choose a pixel scale of $0''.06$ for the spatial information.

We carefully inspect each exposure frame to decide whether they should be included in the stacking procedure. The observations were not centered properly as the guide star selected by the observatory was a binary system, introducing a large offset ($1''.4$ towards SE; Maiolino et al. 2023). We find in 7 frames (#1, 3, 5, 6, 8, 9, 10) the extended CIII] emission with a radius of $\sim 0''.3$ is covered within the field-of-view while the other 3 frames (#2, 4, 7) are not used in this study. We identify potential data artefacts for 3 frames (#3, 8, 10) among the 7 frames. In this study, we mainly discuss the results based on the stacking data cube for the 4 healthy frames (#1, 5, 6, 9) while the results of seven-frame stack are also presented.

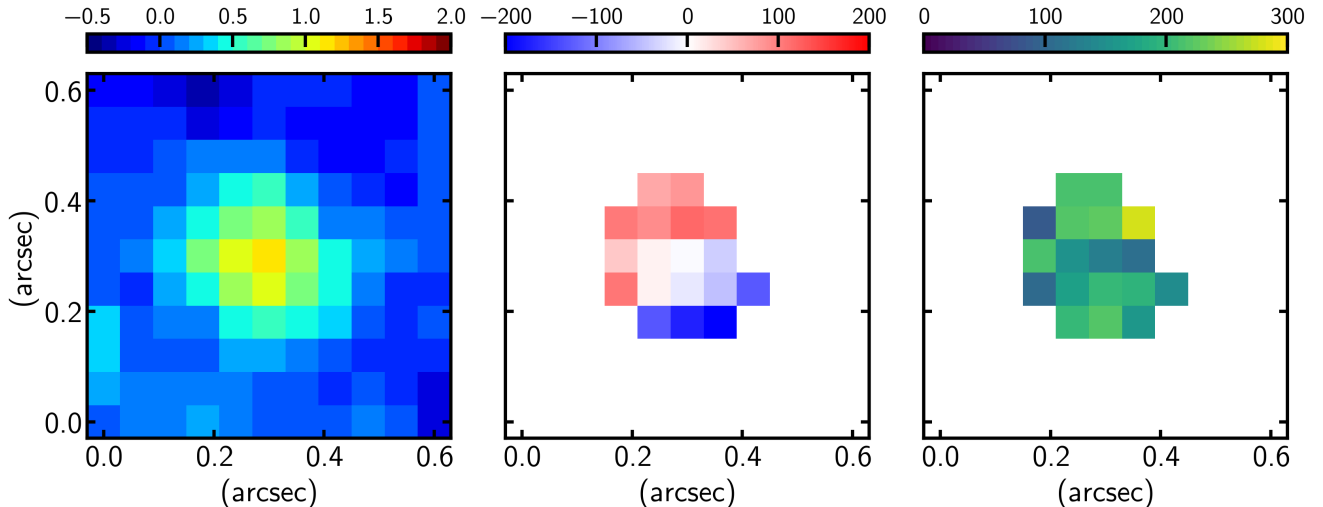


Figure 1. Left to right: the moment-0, -1, and -2 maps derived from the $\text{CIII]}\lambda\lambda 1907, 1909$ emission of GN-z11. The moment-1 and -2 maps are derived by fitting the profile of $\text{CIII]}\lambda\lambda 1907, 1909$ doublets as shown in Figure 3. The colorbar is plotted in an arbitrary unit for the moment-0 map while in the unit of km s^{-1} for moment-1 and -2 maps. There exists a spatial extension and a velocity gradient from NE to SW.

In this study, we mainly examine $\text{CIII]}\lambda\lambda 1907, 1909$ that is the emission with highest signal-to-noise ratio (S/N) within the wavelength coverage of G235M/F170LP and G140M/F100LP grating/filter pairs. We make data cube for $\text{CIII]}\lambda\lambda 1907, 1909$ using the wavelength from $2.2099\mu\text{m}$ to $2.2173\mu\text{m}$ and the pixels in a square region with a radius of 6 pixels from the pixel of $\text{CIII]}\lambda\lambda 1907, 1909$ intensity peak. The map of the continuum is obtained by sigma-clipping and collapsing continuum channels around $\text{CIII]}\lambda\lambda 1907, 1909$ emission. We estimate the noise from the root mean squares (rms) of the fluxes in the IFU field of view with no visible sources.

It is critical to characterize the point-spread-function (PSF) and line-spread-function (LSF) of NIRSpec IFU in the analysis of kinematics. We utilize the observation data of star G-191-B2B taken on 15th of September 2023 under the calibration program 1537 (PI: Karl Gordon). We reduce the data taken with G235M/F170LP following the procedures mentioned above. The data cube of G 191-B2B is cropped to have the same dimension and wavelength range as that of $\text{CIII]}\lambda\lambda 1907, 1909$ to represent the PSF. We also apply the same data reduction procedure on the NIRSpec IFU observations of planetary nebula IRAS-05248-7007 conducted on 1st of August 2023 under the calibration program 1492 (PI: Tracy Beck). We investigate the emission line of the planetary nebula in the same manner as [Isobe et al. \(2023a\)](#). We obtain instrumental broadening of $\sigma_{\text{inst}} = 8.9 \text{ \AA}$ that is consistent with the one of NIRSpec MSA using G235M/F170LP estimated by [Isobe et al. \(2023a\)](#).

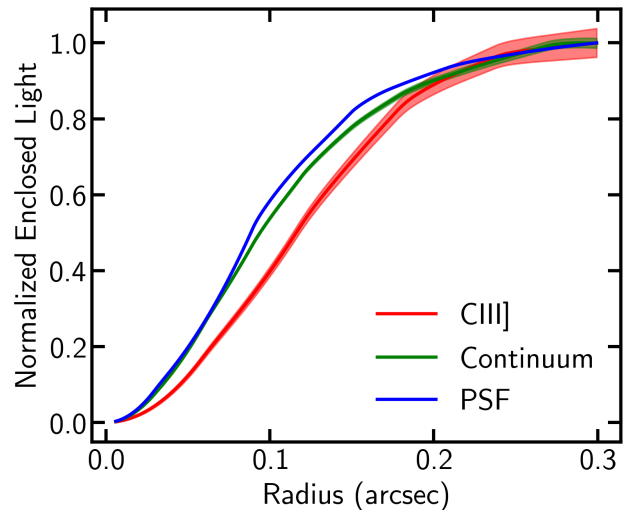


Figure 2. Radial profile of the enclosed light of $\text{CIII]}\lambda\lambda 1907, 1909$ and continuum compared to the shape of PSF. Shaded areas indicate the uncertainties. The $\text{CIII]}\lambda\lambda 1907, 1909$ is more extended than continuum and PSF enabling the analysis of kinematics.

3. ANALYSIS AND RESULTS

3.1. Morphology

We make the narrow band image or the so-called moment-0 map of $\text{CIII]}\lambda\lambda 1907, 1909$ by summing up the data cube in the wavelength direction within the velocity range of -500 km s^{-1} to 800 km s^{-1} around the centroid of $\text{CIII]}\lambda\lambda 1907, 1909$. The moment-0 map in the left panel of Figure 1 shows a slight spatial extension from NE to SW, which is consistent with the descriptions in [Maiolino et al. \(2023\)](#). However, the funnel-shaped geometry ex-

Table 1. Dynamical Properties of GN-z11

Property	Value
Morphology Fitting	
Half-light radius R_e [pc]	294 ± 45
Position angle θ [deg]	247 ± 12
Axial ratio b/a	0.35 ± 0.30
Observed Kinematic Ratio	
Observed velocity difference Δv_{obs} [km s^{-1}]	366^{+62}_{-68}
Median velocity dispersion σ_{med} [km s^{-1}]	122^{+3}_{-83}
$\Delta v_{\text{obs}}/2\sigma_{\text{med}}$	$1.50^{+1.05}_{-0.28}$
Forward Modeling	
Half-light radius R_e [pc]	342^{+31}_{-32}
Position angle θ [deg]	220^{+18}_{-14}
Inclination i [deg]	69 ± 16
Rotational velocity v_{rot} [km s^{-1}]	376^{+110}_{-151}
Velocity dispersion σ_v [km s^{-1}]	113^{+24}_{-48}
v_{rot}/σ_v	$3.33^{+1.72}_{-1.50}$

tended towards the SW is not clearly seen in our median stack results after removing the 3 frame affected by the guiding problem. We fit the moment-0 map with a Sersic model using `galfit` (Peng et al. 2002, 2010). The shape of PSF we measure in Section 2 is convolved with the model during the fitting. We obtain a Sersic index of $n < 0.5$ but with large uncertainties. We thus adopt the fiducial fitting result with a $n = 1$ Sersic profile and obtain a half-light radius of $R_e = 294 \pm 45$ pc as shown in Table 1. Tacchella et al. (2023) find the NIRCcam images of GN-z11 are composed of a central unresolved component and an extended exponential component. Effective radius of CIII] is even larger than the extended component ($R_e = 196 \pm 12$ pc) that is composed of more matured stellar population than the central region. In Figure 2, we show the radial profile of CIII] emission that is more extended than those of the continuum and PSF. The enclosed light profile is derived by integrating the fluxes within a series of circular apertures that oversample the moment-0 map. From the enclosed light profile, we derive the half-light radius of $R_e \sim 285$ pc after subtracting the size of PSF, which is consistent with the once derived from `galfit` fitting. The CIII] morphology is clearly extended and resolved, which enables further kinematic analysis.

3.2. Kinematics

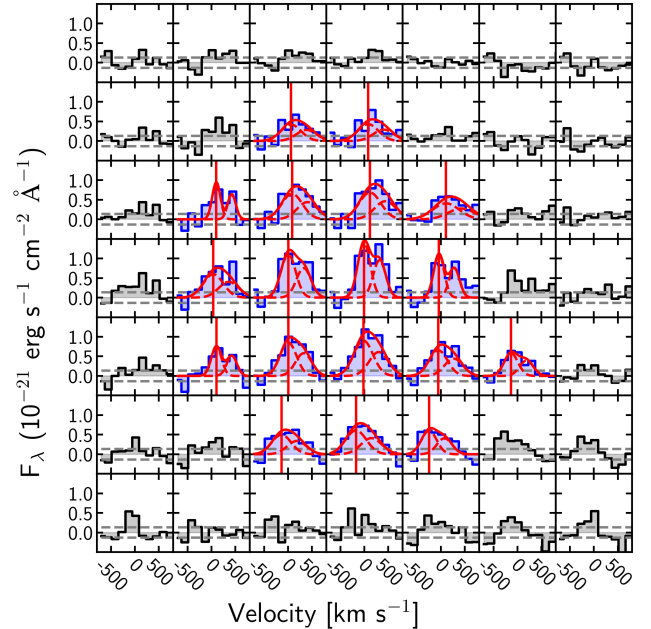


Figure 3. Spectra of CIII] in the central $49 = 7 \times 7$ pixels of Figure 1. In each pixel with $S/N > 6$, we overplot the best-fit profile (red solid curve) composed of two Gaussian components (red dashed curves) that is used to derive the line-of-sight velocity and velocity dispersion. The red vertical line indicates the central velocity of $[\text{CIII}]\lambda 1907$.

We examine the CIII] kinematics by calculating the moment-1 and -2 maps that represent the line-of-sight velocity and velocity dispersion, respectively. Instead of the method by summing up the velocity weighted by the fluxes (e.g., Walter et al. 2008), we adopt a method of profile fitting to the spectrum in each pixel as shown in Figure 3. The profile fitting method on high S/N pixels is more robust against the fluctuations of flux especially at the wavelength channels that correspond to large velocity offset. We select spaxels with a $S/N > 6$ that can be fitted reliably. Because CIII] emission is a doublet, we fit the emission line with two Gaussian components with the constraints of: 1) flux ratio of $[\text{CIII}]\lambda 1907/[\text{CIII}]\lambda 1909 = 1.48$ (Kewley et al. 2019; see Section 3.3 for further discussions), 2) velocity offset between the two centroids fixed to the one at rest-frame, 3) identical line widths larger than the LSF dispersion of $\sigma_{\text{inst}} = 8.9 \text{ \AA}$. By conducting the profile fitting to the integrated spectrum of $S/N > 6$ spaxels, we find the central wavelength of $[\text{CIII}]\lambda 1907$ to be $2.2127 \mu\text{m}$ corresponding to the redshift of 10.605 that is defined as the systematic velocity. As shown in the middle panel of Figure 1, there is a clear velocity gradient from NE to SW consistent with the CIII] morphology. We measure a maximum observed velocity difference of $\Delta v_{\text{obs}} = 366^{+62}_{-68} \text{ km s}^{-1}$ and a median velocity disper-

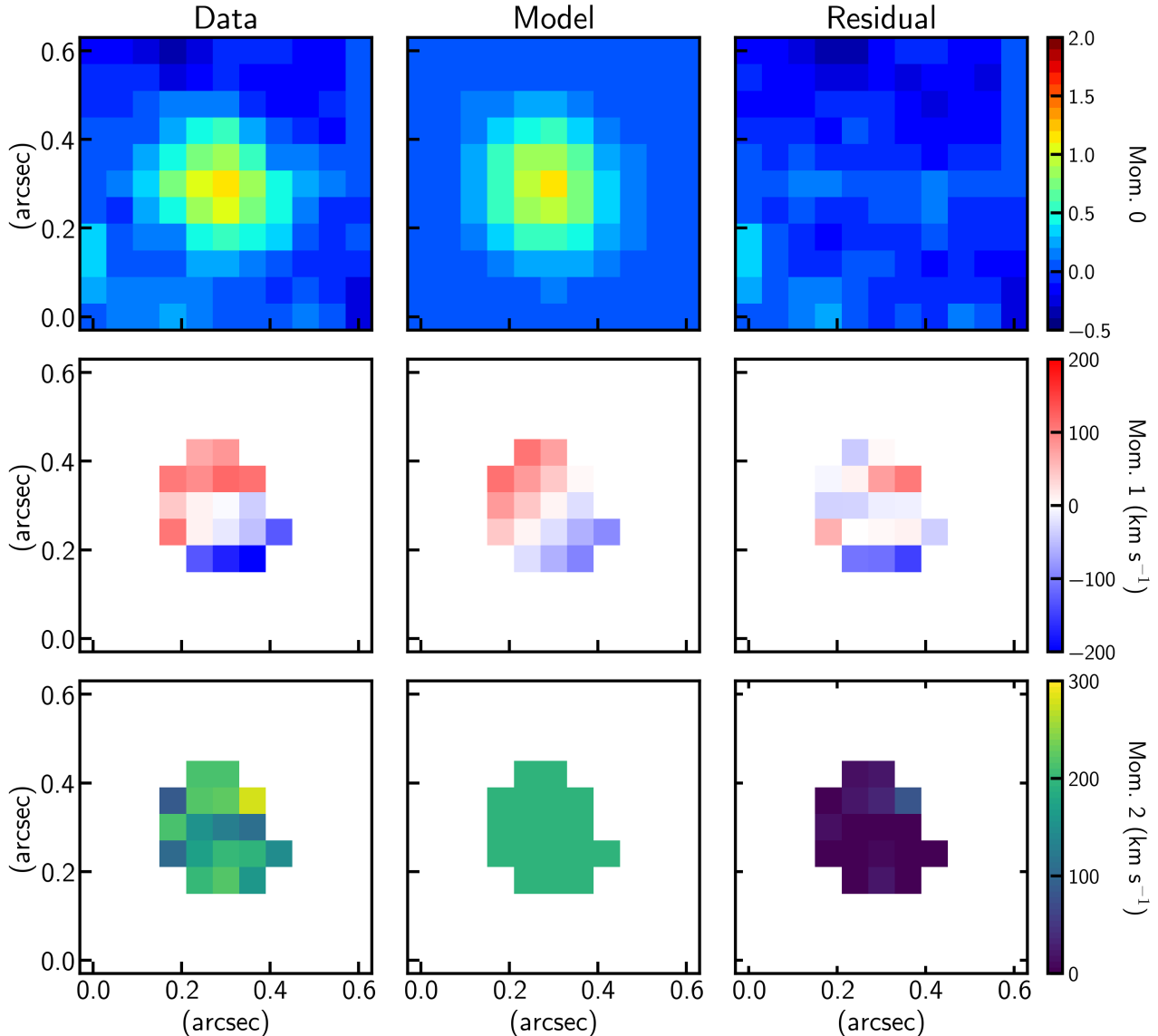


Figure 4. Moment maps compared with the best-fit rotation disk model. Left to right: observed data, GalPak^{3D} model, and the residuals.

tion of $\sigma_{\text{med}} = 122_{-83}^{+3}$ km s⁻¹. The velocity dispersion are the line width σ quadratically subtracted by the σ_{inst} . This value is likely an upper limit because the emission line only marginally resolved compared to the LSF dispersion of ~ 120 km s⁻¹. Here we report the observed kinematic ratio of $\Delta v_{\text{obs}}/2\sigma_{\text{med}} = 1.50$ that is possibly given by a rotational dominated disk.

Assuming the velocity gradient is given by disk rotation, we conduct forward modelling using a software named GalPak^{3D} (Bouché et al. 2015). GalPak^{3D} allows us to fit 3d data cube of doublets assuming a fixed flux ratio and convolve the dynamical model with the PSF shape we derive in Section 2. We choose a thick disk model with the disk height equals to 30% of the

effective radius. The surface brightness is an exponential function of radius, i.e., Sersic profile with a Sersic index of $n = 1$. The choice of the surface brightness profile and disk height is consistent with the modelling result of CIII] morphology. We choose the arctan rotation curve with two parameters, maximum rotation velocity (v_{rot}) and turn-over radius (r_v):

$$v(r) = v_{\text{rot}} \frac{2}{\pi} \arctan(r/r_v). \quad (1)$$

The disk model consists of 10 parameters in total that are x- and y-coordinates of the center, total flux, effective radius (r_e), r_v , inclination (i), position angle, systemic velocity, v_{rot} , and intrinsic dispersion (σ_v). We fix the prior to the uniform distributions whose lower

and upper boundaries are given by the galfit modeling of CIII] morphology. The intrinsic dispersion is free from the broadening given by instrument, the local isotropic velocity dispersion driven by disk self-gravity, and the mixture of the line-of-sight velocities due to the disk thickness (Bouché et al. 2015), and the blending of CIII] doublets. The best-fit model and the residuals of moment maps are presented in Figure 4. While the velocity gradient can be explained by the best-fit model, there still remain residuals on the moment-1 maps possible given by complex dynamical component that is not resolved by the current data. The dynamical properties are shown in Table 1 with the uncertainties obtained by applying forward modelling above on 200 data cubes generated by Monte-Carlo method. We obtain $v_{\text{rot}}/\sigma_v \gtrsim 1$ featuring a rotation dominated disk in GN-z11.

The results above are based on the stacked data cube for 4 healthy frames. Although we find potential data artefacts in the other 3 frames (see Section 2), we also conduct the same analysis on the seven-frame stack and obtain similar results, such as $\Delta v_{\text{obs}} = 238^{+78}_{-67}$ km s⁻¹, $\sigma_{\text{med}} = 77^{+68}_{-77}$ km s⁻¹, $v_{\text{rot}} = 361^{+184}_{-179}$ km s⁻¹, and $\sigma_v = 75^{+22}_{-52}$ km s⁻¹. We adopt the results derived from the four-frame stack as the fiducial values for further discussions.

3.3. Velocity gradient explained by flux ratio variation?

The flux ratio of [CIII]λ1907/CIII]λ1909 is sensitive to the electron density between $n_e = 10^2 - 10^5$ cm⁻³. We examine the flux ratio based on the ionization models of (Kewley et al. 2019) with electron temperature $T_e = 10^4$ K. In Figure 5, we presents spectra of CIII] integrated for all S/N > 6 pixels, those on the NE, and those on the SW together with the best-fit profiles with flux ratio [CIII]λ1907/CIII]λ1909 as a free parameter. To examine the influence of flux ratio on the central wavelengths, we also conduct fitting with flux ratio [CIII]λ1907/CIII]λ1909 fixed to 0.588 ($n_e = 10^5$ cm⁻³) and 1.48 ($n_e < 100$ cm⁻³). Changing the flux ratio results in a velocity difference of $\lesssim 100$ km s⁻¹. The velocity difference between the NE to SW pixels cannot be explained by the variation of flux ratios as shown in Figure 5, which confirms the velocity gradient presented in Figure 1.

We obtain [CIII]λ1907/CIII]λ1909 = 1.12 corresponding to $n_e \sim 10^4$ cm⁻³ from the best-fit profile of the integrated spectrum. Relatively high electron density of $\gtrsim 10^3$ cm⁻³ is consistent with reshift evolution of n_e up to $z \sim 9$ discussed in Isobe et al. (2023a). Particularly, the peak of [CIII]λ1907 appears to be lower than that of CIII]λ1909 (Figure 3), which is a hint of high

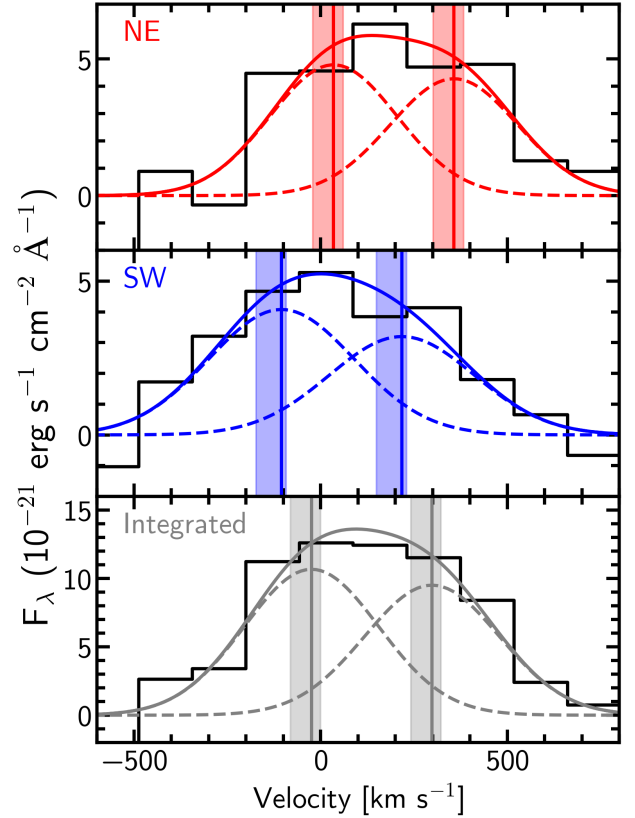


Figure 5. Integrated CIII] spectra of S/N > 6 pixels on the NE (top), SW (middle), and the whole area (bottom) of GN-z11. In the same manner as Figure 3, we show the best-fit profile but with flux ratio [CIII]λ1907/CIII]λ1909 as a free parameter. The solid vertical lines indicate the centroids of [CIII]λ1907 and CIII]λ1909 obtained from the best-fit profile. The left and right boundaries of the shaded areas are obtained from the best-fit profiles with flux ratio fixed to 0.588 ($n_e = 10^5$ cm⁻³) and 1.48 ($n_e = 100$ cm⁻³), respectively. The velocity offset between the NE and SW pixels cannot be explained by the variation of flux ratio.

electron density possibly given by the central black hole (Maiolino et al. 2023, 2024). However, we obtain large 1σ uncertainty = 0.54 on the flux ratio based on the integrated spectrum. The models with $n_e = 10^5$ cm⁻³ or $n_e = 100$ cm⁻³ cannot be ruled out with χ^2 statistics or Bayesian evidence. We thus choose a modest flux ratio of 1.48 that is stable for $n_e \lesssim 10^3$ cm⁻³ to measure the velocities and conduct dynamical modelling.

4. DISCUSSIONS

4.1. Rotation disk at $z > 10$

The ratio between ordered rotation and turbulent motion is often used to indicate a rotation disk. Our estimations of v_{rot}/σ_v are displayed in Figure 6 with a compar-

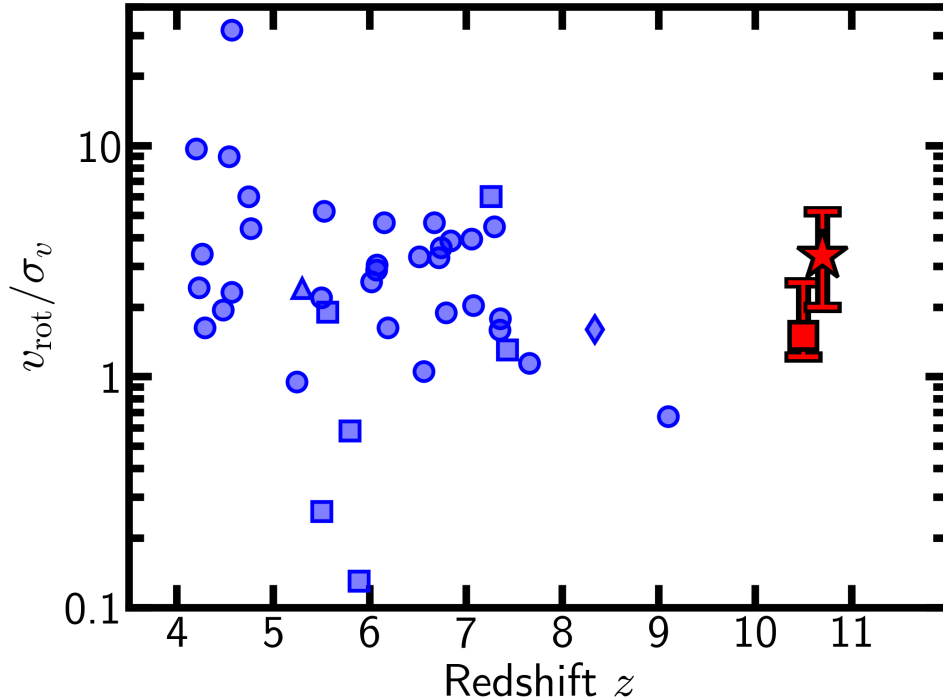


Figure 6. v_{rot}/σ_v of GN-z11 compared to those obtained by previous studies at different redshifts. Our results of GN-z11 are shown with the red star and square that are v_{rot}/σ_v obtained with GalPak^{3D} modelling and the observed kinematic ratio $\Delta v_{\text{obs}}/\sigma_{\text{med}}$, respectively. The blue circles are galaxies whose [CII] kinematics is measured with ALMA taken from Neeleman et al. (2020); Rizzo et al. (2020, 2021); Herrera-Camus et al. (2022); Fraternali et al. (2021); Parlanti et al. (2023). The blue squares are recent JWST results using NIRSpec MSA taken from de Graaff et al. (2023), while the blue triangles and diamonds are taken from Nelson et al. (2023) and Li et al. (2023), respectively, who use NIRCam WFSS.

ison to previous results at different redshifts. Both the observed kinematic ratio and the intrinsic v_{rot}/σ_v agree with the scenario of a rotation dominated disk. Our results are comparable to previous rotating galaxies identified by ground-based sub-millimeter observations (Rizzo et al. 2020, 2021; Fraternali et al. 2021; Herrera-Camus et al. 2022; Tokuoka et al. 2022; Parlanti et al. 2023), rest-frame optical spectroscopy using JWST NIRSpec MSA (de Graaff et al. 2023), and NIRCam WFSS (Nelson et al. 2023; Li et al. 2023). Nevertheless, it is surprising to find a rotation disk at $z > 10$ because galaxies are more likely to be turbulent with increasing redshift due to feedback from massive stars and supernovae (e.g., Pillepich et al. 2019; Yajima et al. 2022, 2023). Simulations of Yajima et al. (2017) show that galactic disks are destroyed due to supernova feedback, while galaxies in simulations with no feedback or lower SF efficiency models can sustain a galactic disk. Recent JWST results of massive luminous galaxies found at $z > 10$ (e.g., Donnan et al. 2023; Harikane et al. 2023, 2024) suggest lack of suppression on star formation. High electron density such found by Isobe et al. (2023a) could be an evidence of efficient cooling in which case feedback becomes inef-

ficient. Dekel et al. (2023) also discuss that high densities and low metallicities in galaxies at $z \gtrsim 10$ result in a high star formation efficiency with feedback-free starbursts. The scenario of weak feedback is consistent with GN-z11 being luminous and rotational dominated.

In Figure 7, we examine mass dependence of the rotation velocity and velocity dispersion combining previous observations and our results of GN-z11. We adopt the stellar mass $\log(M_*/M_\odot) = 9.1_{-0.4}^{+0.3}$ of GN-z11 derived by Tacchella et al. (2023). GN-z11 shows comparable rotation velocity and velocity dispersion to some previous reported high- z galaxies, but possibly larger than those with similar stellar mass of $10^9 M_\odot$. Since the [CII] doublets are only marginally resolved with moderate S/N and spectral resolution, we cannot rule out the possibility that the v_{rot} and σ_v of GN-z11 are overestimated even with our best efforts. Fortunately, GN-z11 will be observed with the $R \sim 2700$ JWST NIRSpec high resolution gratings in the coming cycle-3 missions. Nevertheless, it is possible that GN-z11 has v_{rot} and σ_v larger than those of $z \sim 2$ star forming galaxies (Förster Schreiber et al. 2018) and offsetted from the local Tully-

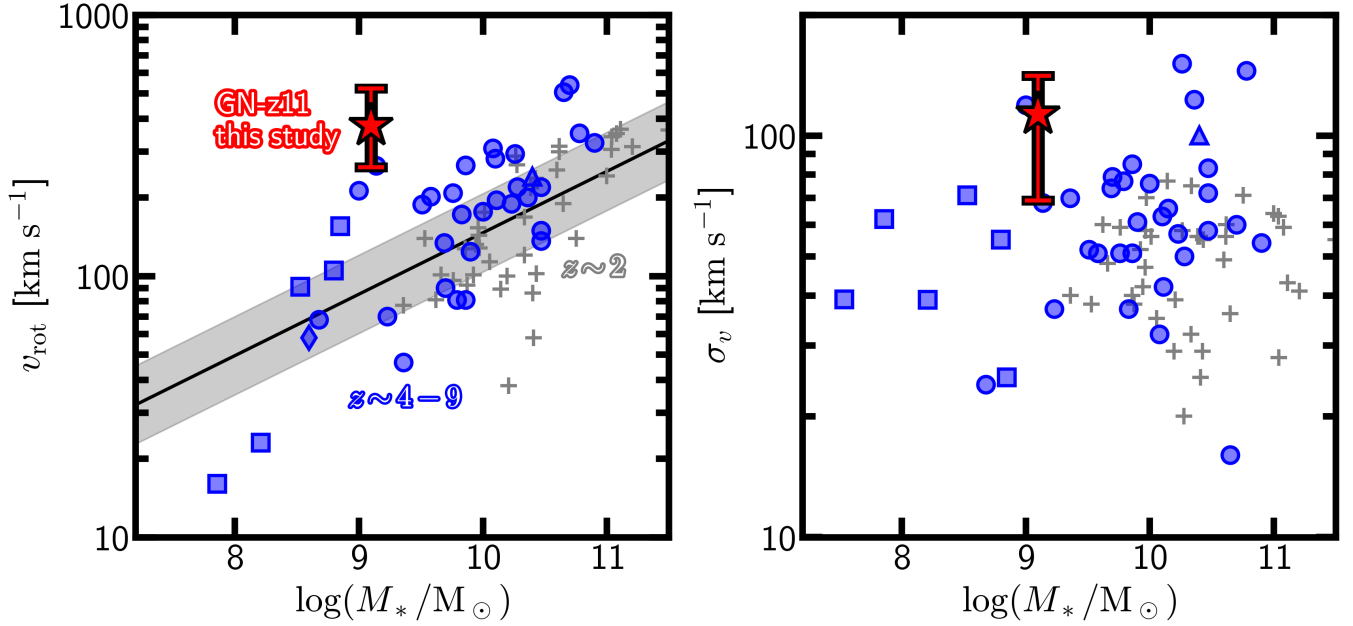


Figure 7. Rotation velocity and velocity dispersion as a function of stellar mass. The symbols are the same as those in Figure 6. The grey crosses are $z \sim 2$ galaxies taken from Förster Schreiber et al. (2018). The grey line on the left panel indicates the Tully-Fisher relation calculated by Di Teodoro et al. (2021).

Fisher relation (e.g., Di Teodoro et al. 2021), which can be explained by the compactness of GNz-11.

Equation (12) of Burkert et al. 2016):

$$v_c^2(r) = v(r)^2 + 2\sigma_v^2 \times \left(\frac{r}{R_d}\right), \quad (2)$$

where $R_d = R_e/1.68$ is the disk scale height. We obtain $v_c(2R_e) = 385^{+86}_{-101}$ km s⁻¹ at the radius that roughly corresponds to the extension of CIII] investigated by this study. This circular velocity is compared with the circular velocity at the virial radius (r_{200}) of the dark matter halo that can be calculated from the halo mass (M_h) using the following equations (Mo & White 2002):

$$v_c(r_{200}) = \left(\frac{GM_h}{r_{200}}\right)^{1/2}, \quad (3)$$

$$r_{200} = \left(\frac{GM_h}{100\Omega_m H_0^2}\right)^{1/3} (1+z)^{-1}. \quad (4)$$

We adopt the $z \sim 8$ stellar mass – halo mass relation from Behroozi et al. (2019) and scale it to match the $z \sim 10$ relation, as the stellar mass of GN-z11 is not well probed by the $z \sim 10$ relation (see Figure 9 of Behroozi et al. 2019). We obtain $M_h = 1.35^{+0.56}_{-0.67} \times 10^{11} M_\odot$ (c.f., Scholtz et al. 2023; Ferrara 2023) and $v_c(r_{200}) = 205^{+28}_{-34}$ km s⁻¹. As shown in Figure 8, $v_c(2R_e)$ is surprisingly larger than $v_c(r_{200})$ with at least 1σ significance. The peaked velocity in the inner radius is consistent with the model shown in Kimm et al. (2015) with no thermal or mechanical feedback, instead of the strong feedback model that would introduce a smoothly rising velocity

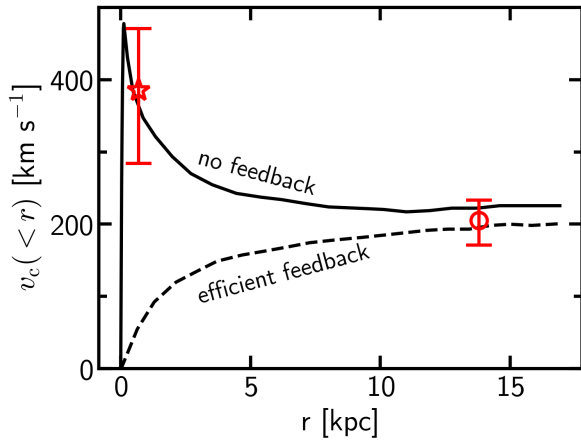


Figure 8. Circular velocities of GN-z11 at $2R_e$ (red star) and virial radius of the dark matter halo (red circle). The black lines are the simulation predictions of Kimm et al. (2015) with a velocity offset for presentation purpose. The peaked v_c in inner radius is consistent with the model of no thermal/mechanical feedback.

To examine the mass concentration of GN-z11, we calculate the circular velocity from the rotation curve of Equation (1) considering the asymmetric drift (see

curve. Such a centrally concentrated mass profile is a favorable explanation for disk formation and efficient star formation as predicted by simulations (e.g., Hopkins et al. 2023).

We further investigate the dynamical state of GN-z11 by firstly estimating the dynamical mass with the following equation:

$$M_{\text{dyn}} = 2.33 \times 10^5 \left(\frac{r}{\text{kpc}} \right) \left(\frac{v_c(r)}{\text{km s}^{-1}} \right)^2. \quad (5)$$

We compare dynamical mass within the effective radius $M_{\text{dyn}}(r < R_e) = 4.3_{-1.7}^{+3.1} \times 10^9 M_\odot$ with the stellar mass and find that the gas mass takes up $\sim 70\%$ of the dynamical mass, assuming negligible mass budget from dark matter. A similar gas mass fraction ($f_{\text{gas}} \sim 0.6$) can be obtained if we adopt the SFR reported by Tacchella et al. (2023) and estimate the gas mass from the star formation rate surface density following the Kennicutt-Schmidt law (Kennicutt 1998). Here we give a rough evaluation of disk instability using the Toomre- Q value:

$$Q = \frac{\sigma_v}{v_{\text{rot}}} \frac{a}{f_{\text{gas}}}, \quad (6)$$

where the parameter a ranges from 1 to 2 depending on the gas distribution. We assume $a = \sqrt{2}$ which corresponds to a disk with constant rotational velocity (Genzel et al. 2011). We find $Q \lesssim 1$ consistent with picture of a rotation disk experiencing gas accretion though disk instability. There is a surprising agreement with the observational results of local dwarf galaxies (e.g., Green et al. 2014; Isobe et al. 2023b; Xu et al. 2024). Green et al. (2014) measure the gas mass for local star forming galaxies and find $M_* \sim 10^9 M_\odot$ galaxies typically have $f_{\text{gas}} \sim 0.5$, which implies $Q \sim 1$ following the calculation of this study. A dynamically unstable rotation disk in GN-z11 is consistent with the picture of efficient gas accretion and star formation, which could be related to weak feedback from central stellar component or AGN.

4.2. Alternative interpretations

We identify a clear velocity gradient using the NIRSpec IFU data of GN-z11 that is well explained by a rotating disk. However, there could be alternative interpretations of the CIII] morphology and kinematics:

- Ionization cone of central black hole (BH). Maiolino et al. (2023) explains the spatial extension of CIII] as the ionization cone of central BH. It is consistent with the scenario of disk rotation, although the CIII] emission may only trace part of the gaseous disk illuminated by the ionization cone.

- Merger. Distinguishing between rotation disk and galaxy mergers has been a longstanding problem for high- z galaxies due to limited spatial resolution. GN-z11 is very compact and may not be well resolved until next-generation facilities such as extremely large telescopes with adaptive optics. With the current observational evidence, the scenario of major merger is not favored for GN-z11 and similar high- z galaxies with compact sizes (see e.g., Ono et al. 2023).
- Outflow. Bunker et al. (2023) find suggestions of galactic outflows from the velocity shift of Ly α . Ferrara (2023) obtain a fiducial terminal velocity of 555 km s^{-1} for the outflows that composed of highly ionized gas. However, outflow signatures are not seen in the relatively bright CIII] or He II λ 1640 emission. Contributions of outflow to the observed CIII] kinematics is likely weak.

5. SUMMARY

In this paper we investigate the dynamics of GN-z11, a luminous galaxy at $z = 10.60$. We carefully analyze the public deep integral field spectroscopy (IFS) data taken with JWST NIRSpec IFU and exploit the spatial and spectral resolution to determine the dynamical properties of GN-z11. Our findings are summarized below:

- We carefully investigate the CIII] λ 1907, 1909 emission that traces ionized gas. The half-light radius of the CIII] emitting gas disk is only 294 ± 45 pc but spatially extended significantly beyond the PSF in contrast with the GN-z11's compact UV-continuum morphology.
- The spatially extended CIII] emission of GN-z11 shows a velocity gradient, red- and blue-shifted components in the NE and SW directions, respectively, which cannot be explained by the variation of [CIII] λ 1907/CIII] λ 1909 line ratios. We perform forward modeling with GalPak^{3D}, including the effects of PSF smearing and line blending, and find that the best-fit model is a nearly edge-on disk with a rotation velocity of $v_{\text{rot}} = 376_{-151}^{+110} \text{ km s}^{-1}$, a velocity dispersion of $\sigma_v = 113_{-48}^{+24} \text{ km s}^{-1}$. Both the observed kinematic ratio $\Delta v_{\text{obs}}/2\sigma_{\text{med}} = 1.50$ and the intrinsic $v_{\text{rot}}/\sigma_v = 3.3_{-1.5}^{+1.7}$ would indicate a rotation-dominated disk.
- The rotation velocity and velocity dispersion of GN-z11 is comparable to $4 < z < 9$ galaxies previously reported by ground-based sub-millimeter observations and JWST, but possibly larger than

those with similar stellar mass of $10^9 M_{\odot}$. Observations with better S/N and resolution are required to confirm this result.

- The disk rotation velocity is faster than the circular velocity at the virial radius, $v_c(r_{200}) = 205_{-34}^{+28}$ km s⁻¹, suggesting a compact disk produced under weak feedback such predicted in numerical simulations. Our results would suggest a fast-rotating gaseous disk at $z > 10$ whose center possesses luminous stellar components or AGN providing weak feedback.

This work is based on observations made with the NASA/ESA/CSA James Webb Space Telescope. The data were obtained from the Mikulski Archive for Space Telescopes at the Space Telescope Science Institute, which is operated by the Association of Universities for Research in Astronomy, Inc., under NASA contract NAS 5-03127 for JWST. These observations are associated with programs 1429, 1537, and 4426. We thank the

research team led by Roberto Maiolino for developing their observing program of GN-z11. We thank Yuzo Ishikawa for the discussions on data analysis of JWST NIRspec IFU. We are grateful to staff of the James Webb Space Telescope Help Desk for letting us know useful information. This work was supported by the joint research program of the Institute for Cosmic Ray Research (ICRR), University of Tokyo. This publication is based upon work supported by the World Premier International Research Center Initiative (WPI Initiative), MEXT, Japan. M.O., H.Y., H.F., K.N., Y.H., and Y.I. are supported by JSPS KAKENHI Grant Nos. 20H00180/21H04467, 21H04489, 3K13139, 20K22373, 21K13953, and 24KJ0202 respectively. H.Y. is supported by JST FOREST Program, Grant Number JP-MJFR202Z.

Software: astropy (Astropy Collaboration et al. 2013, 2018), reproject (Robitaille et al. 2023), galfit (Peng et al. 2002, 2010), GalPak^{3D} (Bouché et al. 2015)

REFERENCES

- Arrabal Haro, P., Dickinson, M., Finkelstein, S. L., et al. 2023a, ApJL, 951, L22, doi: [10.3847/2041-8213/acdd54](https://doi.org/10.3847/2041-8213/acdd54)
- . 2023b, Nature, 622, 707, doi: [10.1038/s41586-023-06521-7](https://doi.org/10.1038/s41586-023-06521-7)
- Astropy Collaboration, Robitaille, T. P., Tollerud, E. J., et al. 2013, A&A, 558, A33, doi: [10.1051/0004-6361/201322068](https://doi.org/10.1051/0004-6361/201322068)
- Astropy Collaboration, Price-Whelan, A. M., Sipőcz, B. M., et al. 2018, AJ, 156, 123, doi: [10.3847/1538-3881/aabc4f](https://doi.org/10.3847/1538-3881/aabc4f)
- Behroozi, P., Wechsler, R. H., Hearin, A. P., & Conroy, C. 2019, MNRAS, 488, 3143, doi: [10.1093/mnras/stz1182](https://doi.org/10.1093/mnras/stz1182)
- Böker, T., Arribas, S., Lützgendorf, N., et al. 2022, A&A, 661, A82, doi: [10.1051/0004-6361/202142589](https://doi.org/10.1051/0004-6361/202142589)
- Bouché, N., Carfantan, H., Schroetter, I., Michel-Dansac, L., & Contini, T. 2015, AJ, 150, 92, doi: [10.1088/0004-6256/150/3/92](https://doi.org/10.1088/0004-6256/150/3/92)
- Bouwens, R. J., Illingworth, G. D., González, V., et al. 2010, ApJ, 725, 1587, doi: [10.1088/0004-637X/725/2/1587](https://doi.org/10.1088/0004-637X/725/2/1587)
- Bunker, A. J., Saxena, A., Cameron, A. J., et al. 2023, A&A, 677, A88, doi: [10.1051/0004-6361/202346159](https://doi.org/10.1051/0004-6361/202346159)
- Burkert, A., Förster Schreiber, N. M., Genzel, R., et al. 2016, ApJ, 826, 214, doi: [10.3847/0004-637X/826/2/214](https://doi.org/10.3847/0004-637X/826/2/214)
- Curtis-Lake, E., Carniani, S., Cameron, A., et al. 2023, Nature Astronomy, 7, 622, doi: [10.1038/s41550-023-01918-w](https://doi.org/10.1038/s41550-023-01918-w)
- de Graaff, A., Rix, H.-W., Carniani, S., et al. 2023, arXiv e-prints, arXiv:2308.09742, doi: [10.48550/arXiv.2308.09742](https://doi.org/10.48550/arXiv.2308.09742)
- Dekel, A., Sari, R., & Ceverino, D. 2009, ApJ, 703, 785, doi: [10.1088/0004-637X/703/1/785](https://doi.org/10.1088/0004-637X/703/1/785)
- Dekel, A., Sarkar, K. C., Birnboim, Y., Mandelker, N., & Li, Z. 2023, MNRAS, 523, 3201, doi: [10.1093/mnras/stad1557](https://doi.org/10.1093/mnras/stad1557)
- D'Eugenio, F., Perez-Gonzalez, P., Maiolino, R., et al. 2023, arXiv e-prints, arXiv:2308.06317, doi: [10.48550/arXiv.2308.06317](https://doi.org/10.48550/arXiv.2308.06317)
- Di Teodoro, E. M., Posti, L., Ogle, P. M., Fall, S. M., & Jarrett, T. 2021, MNRAS, 507, 5820, doi: [10.1093/mnras/stab2549](https://doi.org/10.1093/mnras/stab2549)
- Donnan, C. T., McLeod, D. J., Dunlop, J. S., et al. 2023, MNRAS, 518, 6011, doi: [10.1093/mnras/stac3472](https://doi.org/10.1093/mnras/stac3472)
- Ferrara, A. 2023, arXiv e-prints, arXiv:2310.12197, doi: [10.48550/arXiv.2310.12197](https://doi.org/10.48550/arXiv.2310.12197)
- Förster Schreiber, N. M., Genzel, R., Bouché, N., et al. 2009, ApJ, 706, 1364, doi: [10.1088/0004-637X/706/2/1364](https://doi.org/10.1088/0004-637X/706/2/1364)
- Förster Schreiber, N. M., Renzini, A., Mancini, C., et al. 2018, ApJS, 238, 21, doi: [10.3847/1538-4365/aadd49](https://doi.org/10.3847/1538-4365/aadd49)
- Fraternali, F., Karim, A., Magnelli, B., et al. 2021, A&A, 647, A194, doi: [10.1051/0004-6361/202039807](https://doi.org/10.1051/0004-6361/202039807)
- Genzel, R., Newman, S., Jones, T., et al. 2011, ApJ, 733, 101, doi: [10.1088/0004-637X/733/2/101](https://doi.org/10.1088/0004-637X/733/2/101)

- Green, A. W., Glazebrook, K., McGregor, P. J., et al. 2014, *MNRAS*, 437, 1070, doi: [10.1093/mnras/stt1882](https://doi.org/10.1093/mnras/stt1882)
- Harikane, Y., Nakajima, K., Ouchi, M., et al. 2024, *ApJ*, 960, 56, doi: [10.3847/1538-4357/ad0b7e](https://doi.org/10.3847/1538-4357/ad0b7e)
- Harikane, Y., Ouchi, M., Oguri, M., et al. 2023, *ApJS*, 265, 5, doi: [10.3847/1538-4365/acaaa9](https://doi.org/10.3847/1538-4365/acaaa9)
- Herrera-Camus, R., Förster Schreiber, N. M., Price, S. H., et al. 2022, *A&A*, 665, L8, doi: [10.1051/0004-6361/202142562](https://doi.org/10.1051/0004-6361/202142562)
- Hopkins, P. F., Kereš, D., Murray, N., Quataert, E., & Hernquist, L. 2012, *MNRAS*, 427, 968, doi: [10.1111/j.1365-2966.2012.21981.x](https://doi.org/10.1111/j.1365-2966.2012.21981.x)
- Hopkins, P. F., Gurvich, A. B., Shen, X., et al. 2023, *MNRAS*, 525, 2241, doi: [10.1093/mnras/stad1902](https://doi.org/10.1093/mnras/stad1902)
- Isobe, Y., Ouchi, M., Nakajima, K., et al. 2023a, *ApJ*, 956, 139, doi: [10.3847/1538-4357/acf376](https://doi.org/10.3847/1538-4357/acf376)
- . 2023b, *ApJ*, 951, 102, doi: [10.3847/1538-4357/accc87](https://doi.org/10.3847/1538-4357/accc87)
- Jakobsen, P., Ferruit, P., Alves de Oliveira, C., et al. 2022, *A&A*, 661, A80, doi: [10.1051/0004-6361/202142663](https://doi.org/10.1051/0004-6361/202142663)
- Kennicutt, Robert C., J. 1998, *ApJ*, 498, 541, doi: [10.1086/305588](https://doi.org/10.1086/305588)
- Kewley, L. J., Nicholls, D. C., Sutherland, R., et al. 2019, *ApJ*, 880, 16, doi: [10.3847/1538-4357/ab16ed](https://doi.org/10.3847/1538-4357/ab16ed)
- Kimm, T., Cen, R., Devriendt, J., Dubois, Y., & Slyz, A. 2015, *MNRAS*, 451, 2900, doi: [10.1093/mnras/stv1211](https://doi.org/10.1093/mnras/stv1211)
- Li, Z., Cai, Z., Sun, F., et al. 2023, arXiv e-prints, arXiv:2310.09327, doi: [10.48550/arXiv.2310.09327](https://doi.org/10.48550/arXiv.2310.09327)
- Maiolino, R., Uebler, H., Perna, M., et al. 2023, arXiv e-prints, arXiv:2306.00953, doi: [10.48550/arXiv.2306.00953](https://doi.org/10.48550/arXiv.2306.00953)
- Maiolino, R., Scholtz, J., Witstok, J., et al. 2024, *Nature*, 627, 59, doi: [10.1038/s41586-024-07052-5](https://doi.org/10.1038/s41586-024-07052-5)
- Mo, H. J., & White, S. D. M. 2002, *MNRAS*, 336, 112, doi: [10.1046/j.1365-8711.2002.05723.x](https://doi.org/10.1046/j.1365-8711.2002.05723.x)
- Naab, T., & Ostriker, J. P. 2017, *ARA&A*, 55, 59, doi: [10.1146/annurev-astro-081913-040019](https://doi.org/10.1146/annurev-astro-081913-040019)
- Neeleman, M., Prochaska, J. X., Kanekar, N., & Rafelski, M. 2020, *Nature*, 581, 269, doi: [10.1038/s41586-020-2276-y](https://doi.org/10.1038/s41586-020-2276-y)
- Nelson, D., Pillepich, A., Springel, V., et al. 2019, *MNRAS*, 490, 3234, doi: [10.1093/mnras/stz2306](https://doi.org/10.1093/mnras/stz2306)
- Nelson, E. J., Brammer, G., Gimenez-Arteaga, C., et al. 2023, arXiv e-prints, arXiv:2310.06887, doi: [10.48550/arXiv.2310.06887](https://doi.org/10.48550/arXiv.2310.06887)
- Oesch, P. A., Brammer, G., van Dokkum, P. G., et al. 2016, *ApJ*, 819, 129, doi: [10.3847/0004-637X/819/2/129](https://doi.org/10.3847/0004-637X/819/2/129)
- Ono, Y., Harikane, Y., Ouchi, M., et al. 2023, *ApJ*, 951, 72, doi: [10.3847/1538-4357/acd44a](https://doi.org/10.3847/1538-4357/acd44a)
- Parlanti, E., Carniani, S., Pallottini, A., et al. 2023, *A&A*, 673, A153, doi: [10.1051/0004-6361/202245603](https://doi.org/10.1051/0004-6361/202245603)
- Peng, C. Y., Ho, L. C., Impey, C. D., & Rix, H.-W. 2002, *AJ*, 124, 266, doi: [10.1086/340952](https://doi.org/10.1086/340952)
- . 2010, *AJ*, 139, 2097, doi: [10.1088/0004-6256/139/6/2097](https://doi.org/10.1088/0004-6256/139/6/2097)
- Perna, M., Arribas, S., Marshall, M., et al. 2023, *A&A*, 679, A89, doi: [10.1051/0004-6361/202346649](https://doi.org/10.1051/0004-6361/202346649)
- Pillepich, A., Nelson, D., Springel, V., et al. 2019, *MNRAS*, 490, 3196, doi: [10.1093/mnras/stz2338](https://doi.org/10.1093/mnras/stz2338)
- Planck Collaboration, Aghanim, N., Akrami, Y., et al. 2020, *A&A*, 641, A6, doi: [10.1051/0004-6361/201833910](https://doi.org/10.1051/0004-6361/201833910)
- Rauscher, B. J. 2024, *PASP*, 136, 015001, doi: [10.1088/1538-3873/ad1b36](https://doi.org/10.1088/1538-3873/ad1b36)
- Rizzo, F., Vegetti, S., Fraternali, F., Stacey, H. R., & Powell, D. 2021, *MNRAS*, 507, 3952, doi: [10.1093/mnras/stab2295](https://doi.org/10.1093/mnras/stab2295)
- Rizzo, F., Vegetti, S., Powell, D., et al. 2020, *Nature*, 584, 201, doi: [10.1038/s41586-020-2572-6](https://doi.org/10.1038/s41586-020-2572-6)
- Robitaille, T., Ginsburg, A., Mumford, S., et al. 2023, *astropy/reproject*: v0.11.0, v0.11.0, Zenodo, doi: [10.5281/zenodo.7950746](https://doi.org/10.5281/zenodo.7950746)
- Scholtz, J., Witten, C., Laporte, N., et al. 2023, arXiv e-prints, arXiv:2306.09142, doi: [10.48550/arXiv.2306.09142](https://doi.org/10.48550/arXiv.2306.09142)
- Tacchella, S., Eisenstein, D. J., Hainline, K., et al. 2023, *ApJ*, 952, 74, doi: [10.3847/1538-4357/acdbcf6](https://doi.org/10.3847/1538-4357/acdbcf6)
- Tokuoka, T., Inoue, A. K., Hashimoto, T., et al. 2022, *ApJL*, 933, L19, doi: [10.3847/2041-8213/ac7447](https://doi.org/10.3847/2041-8213/ac7447)
- Vayner, A., Zakamska, N. L., Ishikawa, Y., et al. 2023, *ApJ*, 955, 92, doi: [10.3847/1538-4357/ace784](https://doi.org/10.3847/1538-4357/ace784)
- Walter, F., Brinks, E., de Blok, W. J. G., et al. 2008, *AJ*, 136, 2563, doi: [10.1088/0004-6256/136/6/2563](https://doi.org/10.1088/0004-6256/136/6/2563)
- Wisnioski, E., Förster Schreiber, N. M., Wuyts, S., et al. 2015, *ApJ*, 799, 209, doi: [10.1088/0004-637X/799/2/209](https://doi.org/10.1088/0004-637X/799/2/209)
- Xu, Y., Ouchi, M., Isobe, Y., et al. 2024, *ApJ*, 961, 49, doi: [10.3847/1538-4357/ad06ab](https://doi.org/10.3847/1538-4357/ad06ab)
- Yajima, H., Abe, M., Fukushima, H., et al. 2023, *MNRAS*, 525, 4832, doi: [10.1093/mnras/stad2497](https://doi.org/10.1093/mnras/stad2497)
- Yajima, H., Nagamine, K., Zhu, Q., Khochfar, S., & Dalla Vecchia, C. 2017, *ApJ*, 846, 30, doi: [10.3847/1538-4357/aa82b5](https://doi.org/10.3847/1538-4357/aa82b5)
- Yajima, H., Abe, M., Khochfar, S., et al. 2022, *MNRAS*, 509, 4037, doi: [10.1093/mnras/stab3092](https://doi.org/10.1093/mnras/stab3092)